Recent changes in pan-Antarctic surface snowmelt detected by AMSR-E and AMSR2

Lei Zheng[1], Chunxia Zhou[1], Tingjun Zhang[2], Qi Liang[1], Kang Wang[3]

[1]Chinese Antarctic Center of Surveying and Mapping, Wuhan University, Wuhan 430079, China
5 [2]Key Laboratory of Western China's Environmental Systems (Ministry of Education), College of Earth and Environmental Sciences, Lanzhou University, Lanzhou 730000, China
[3]Institute of Arctic and Alpine Research, University of Colorado Boulder, Boulder, Colorado, 80309, USA

Correspondence to: Chunxia Zhou (zhoucx@whu.edu.cn) and Tingjun Zhang (tjzhang@lzu.edu.cn)

10 **Abstract.** Surface snowmelt in the pan-Antarctic, including the Antarctic ice sheet (AIS) and sea ice, is crucial to the mass and energy balance in polar regions and can serve as an indicator of climate change. Here, we investigated the spatial and temporal variations in the surface snowmelt over the entire pan-Antarctic from 2002 to 2017 by using the passive microwave remote sensing data. The stable orbit and appropriate acquisition time of the Advanced Microwave Scanning Radiometer for the Earth Observing System (AMSR-E) and the Advanced Microwave Scanning Radiometer 2 (AMSR2) enable us to take full

15 advantage of the daily brightness temperature (Tb) variations to detect the surface snowmelt. In this study, the difference between AMSR-E/2 ascending and descending 36.5 GHz Tb in vertical polarization (DAV36) was utilized to map the pan-Antarctic snowmelt because it is unaffected by the snow metamorphism. We evaluated the DAV36 algorithm against ground-based measurements and further improved the method over the marginal sea ice zone by excluding the effect of open water. Snowmelt detected by AMSR-E/2 data was more extensive and persistent than that detected by the Special Sensor

20 Microwave/Imager (SSM/I) data. On average, pan-Antarctic early snowmelt onset (EMO) occurs in late September, while continuous melt onset (CMO) occurs in mid-November. Overall, pan-Antarctic surface snowmelt showed a trend (at the 90% confidence level) towards later EMO (0.68 days yr^{-1}) during the 2002-2017 period. Pan-Antarctic CMO was significantly correlated (at the 95% confidence level) with summer Southern Annular Mode (SAM). The decreased surface snowmelt on the AIS was very likely linked with the enhanced summer SAM.

25 ## 1 Introduction

Surface snowmelt on sea ice and ice sheets has a great influence on the energy exchange between the snow surface and atmosphere because wet snow has a lower albedo, and thus absorbs more incoming solar radiation than dry snow (Steffen, 1995). Intense snowmelt leads to the formation of melt ponds on sea ice and ice sheets, which in turn absorb more radiation and induce further snowmelt through melt-albedo feedback (Tanaka et al., 2016; Bell et al., 2018). Meltwater may fill in the

30 ice crevasses on ice sheets and migrate to the ice-bedrock surface, which can induce the acceleration of ice flow (Zwally et al.,

2002; Sundal et al., 2011). Meltwater can also transport heat into crevasses and deepen them, providing the conditions for ice shelves to break up through hydrofracturing (Scambos et al., 2000; van den Broeke, 2005). Therefore, the spatial and temporal dynamics of surface snowmelt on sea ice and ice sheets have a direct effect on mass and energy balances in polar regions (Picard and Fily, 2006; van den Broeke et al., 2009; Stroeve et al., 2014). The timing and extent of surface snowmelt are

5   indicators of changes in polar climate (Intergovernmental Panel on Climate Change (IPCC), 2014), and thus potentially have regional and global climate implications.

In-situ observations of snowmelt are sparse over sea ice and ice sheets due to an unfavorable environment. Remote sensing techniques can provide timely data sets for the monitoring of melt events in polar regions. When a snowpack begins to melt, the most significant change in the electromagnetic properties is an abrupt increase in the dielectric constant, which increases

10   absorption and reduces the penetration depth of microwaves (Ashcraft and Long, 2006). Therefore, snowmelt can be detected via microwave radiometry by identifying the sharp changes in microwave brightness temperatures (Tb) caused by the presence of snow liquid water (Serreze et al., 1993; Liu et al., 2005).

Microwave radiometers can operate regardless of illumination conditions and are insensitive to atmospheric conditions. Most spaceborne passive microwave instruments provide more than two daily passes in polar regions. Scanning Multi-channel

15   Microwave Radiometer (SMMR) 18 GHz and 37 GHz Tb and Special Sensor Microwave/Imager (SSM/I) 19 GHz and 37 GHz Tb have been used to detect surface snowmelt on ice sheets when Tb is above a region-specific or user-defined constant depending on the local snow properties (Ridley, 1993; Zwally and Fiegles, 1994; Mote and Anderson, 1995; Tedesco, 2009). Tb received by satellites is also related to the ground physical temperature, clouds and atmospheric water vapor, which may contaminate melt signals in the Tb time series. Multi-channel methods were developed to minimize these interferences, e.g.,

20   using a gradient ratio or a cross-polarized gradient ratio (XGPR) between 19 GHz and 37 GHz to detect surface snowmelt on sea ice and ice sheets (Abdalati and Steffen, 1995; Markus et al., 2009; Liang et al., 2013; Arndt et al., 2016). Snowmelt can also be recognized based on edge detection or wavelet transform-based technologies by identifying the abrupt changes in Tb values (Joshi et al., 2001; Liu et al., 2005).

Snow grain size increases after the liquid water refreezes. As a result, dry snow Tb decreases during the melt season due to

25   the increase in volume scattering (Markus et al., 2009). Therefore, single-channel methods may fail to identify melt events because of the metamorphic snow structures. Ramage and Isacks (2002, 2003) introduced the SSM/I diurnal amplitude variations (DAV, i.e., the Tb difference between ascending and descending passes) in vertically polarized 37 GHz Tb to investigate the snowmelt timing on the Southeast Alaskan Icefields. The DAV method is unaffected by snow metamorphism in melt detection. This technique has been successfully applied to ice sheets and was proven to be more sensitive to snow

30   liquid water than the XGPR method (Tedesco, 2007; Zheng et al., 2018). Freeze-thaw cycles on the Antarctic sea ice were also successfully detected based on the SSM/I 37 GHz DAV (Willmes et al., 2009). Furthermore, Arndt et al. (2016) distinguished temporary snowmelt from continuous snowmelt on the Antarctic sea ice by combining DAV with the cross-polarized ratio of SSM/I Tb. In these studies, surface snowmelt patterns were not described over the marginal sea ice zone, where the earliest

sea ice retreat was identified (Stammerjohn et al., 2008). DAV may not be strong enough to be identified as melt signals when open water with low Tb emerges in the first-year sea ice zone.

Most of these studies investigated surface snowmelt on sea ice and ice sheets based on SSM/I sensors. However, SSM/I observations show considerable variations in local acquisition time because of orbit degradation (Picard and Fily, 2006). By contrast, the Advanced Microwave Scanning Radiometer for the Earth Observing System (AMSR-E) and the Advanced Microwave Scanning Radiometer 2 (AMSR2) operate in controlled-orbits so that local acquisition time shows little temporal variation (http://www.remss.com/support/crossing-times). AMSR-E/2 measurements with a stable orbit are superior in the analyses of inter-annual snowmelt dynamics. Diurnal melt area in the Antarctic varies approximately as a sinusoid with the peak in the afternoon and the trough in the early morning (Picard and Fily, 2006). AMSR-E/2 can monitor the Antarctic sea ice and ice sheet (referred to as pan-Antarctic) surface snowmelt at the appropriate local acquisition time. Taking 2002-2003 as an example, the local acquisition time of ascending and descending SSM/I Tb products south of 40° S were 19.17±0.44 and 5.45±0.45, respectively, while these values were 14.16±0.20 and 0.88±0.20 for the AMSR-E Tb products. Compared with SSM/I, AMSR-E/2 have more opportunities to detect melt events in the pan-Antarctic due to warmer and colder periods for ascending and descending passes and an expected higher DAV.

Unlike the Arctic sea ice and Greenland ice sheet, pan-Antarctic surface snowmelt is relatively short-lived and patchy (Drinkwater and Liu, 2000; Picard et al., 2007), and has received much less attention. Contrary to the reduction in sea ice extent, thickness and duration in the Arctic, the Antarctic sea ice presented increasing trends in both extent and duration, especially in the Ross Sea (Comiso and Nishio, 2008; Hobbs et al., 2016). Most of the Antarctic sea ice is snow-covered, even in summer when snowmelt occurs (Brandt et al., 2005). Melt ponds are not often observed on the Antarctic sea ice (Ackley et al., 2008). Meltwater on the Antarctic ice sheet (AIS) can refreeze quasi-instantaneously (van den Broeke et al., 2010a) and contributes little to the surface mass balance (The IMBIE team, 2018). Although more than 25% of the AIS has experienced snowmelt since the 1980s, only 2% melts every year (Picard et al., 2007). Melt extent has been decreasing over the AIS since 1987 (Tedesco et al., 2007).

Strong interactions have been found between sea ice and ice sheet surface snowmelt through atmospheric circulation (Stroeve et al., 2017). Surface snowmelt dynamics in the West Antarctic and Antarctic peninsula have been found to be related with the sea ice variations in adjacent seas (Scott et al., 2018; Zheng et al., 2019). Previous studies have separately investigated surface snowmelt on sea ice and ice sheet, which may result in uncertainties in the integrated study. The DAV method has been successfully applied in snowmelt detection on both sea ice (Willmes et al., 2009) and ice sheet (Tedesco, 2007; Zheng et al., 2018). It is worthwhile to estimate snowmelt over the pan-Antarctic based on a uniform approach. The overall objective of this study is to improve the understanding of surface snowmelt over the pan-Antarctic based on the DAV method in three aspects: (1) to detect the pan-Antarctic surface snowmelt at the stable and appropriate local acquisition time based on AMSR-E/2, (2) to improve the performance of the DAV method in the marginal sea ice zone by excluding the effect of open water, and (3) to estimate the pan-Antarctic surface snowmelt as a whole and systematically describe the surface snowmelt patterns and changes from 2002 to 2017.

2 Data sets

2.1 Data from AMSR-E/2

A modified version of the AMSR radiometer, the AMSR-E radiometer, launched aboard the NASA Earth Observing System (EOS) Aqua satellite on 4 May 2002. We obtained the 25 km AMSR-E/Aqua L2A global swath spatially-resampled 36 GHz Tb data from the National Snow and Ice Data Center (NSIDC, www.nsidc.org) (Knowles et al., 2006). AMSR2 aboard the Global Change Observation Mission-Water (GCOM-W1) satellite was launched on 18 May 2012 after AMSR-E ceased operations. As a successor of AMSR-E, AMSR2 shares almost the same satellite orbit and sensor parameters as AMSR-E, and provides continuous measurements for the study of global climate change, energy balance and ecosystems. The 25 km AMSR2 Tb used in this study was provided by the Japan Aerospace Exploration Agency (JAXA, http://suzaku.eorc.jaxa.jp/GCOM/). AMSR-E/2 obtained data over a 1450 km swath. The brightness temperature products at 36.5 GHz in vertical polarization (Tb_{V36}) was used to estimate the pan-Antarctic snowmelt extent and timing in this study.

2.2 Sea ice and atmospheric products

The Bootstrap sea ice concentration (SIC) product was used to mask sea ice in this study (Comiso, 2017). The 25 km daily SIC South Hemisphere product was obtained from the NSIDC (http://nsidc.org/data/nsidc-0079), University of Colorado Boulder. Pixels with SIC greater than 80% for less than 5 days were marked as being ice-free (Markus et al., 2009). For a sea ice pixel, SIC above 15% indicates the presence of sea ice (Meier and Stroeve, 2008).

ERA-Interim is a global reanalysis produced by the European Centre for Medium-Range Weather Forecasts (ECMWF). The ERA-Interim reanalysis includes various surface parameters, describing weather, ocean and land-surface conditions since 1979 (Dee et al., 2011). The 6-hourly air temperature (Tair) from the gridded ERA-Interim reanalysis at 2 m height was used to assist with melt detection based on AMSR-E/2, as well as directly determine snowmelt in this study.

The sea ice product is provided in the NSIDC EASE-Grid projection, which is the same as the AMSR-E/2 products. The 0.5° gridded ERA-Interim reanalysis was reprojected to the NSIDC EASE-Grid, and resampled to the same spatial resolution as the passive microwave measurements (25 km).

3 Methodology

3.1 Tb and liquid water content

According to the Rayleigh-Jeans approximation, Tb is a function of emissivity (ε) and the near-surface physical temperature (Ts) of snow and ice (Zwally, 1977):

$$Tb = \varepsilon Ts \tag{1}$$

Previous studies have emphasized the process that Tb increases when the snowpack starts to melt due to the increase in emissivity. However, Tb decreases after reaching a peak when the volume liquid water is approximately about one percent

(Kang et al., 2014). We investigated the variations in Tb_{V36} with increasing snow liquid water based on the Microwave Emission Model of Multi-layered Snowpack (MEMLS) (Wiesmann and Mätzler, 1999). In the simulations, snow temperature, density and depth in a homogeneous snowpack were set to 273.15 K, 350 kg m^{-3}, and 20 cm, respectively, by referring to Brucker et al. (2010) and Kang et al. (2014). Snow-ice reflectivity at 36.5 GHz was set to 0.045 in vertical polarization according to Powell et al. (2006). The evolution of Tb with increasing liquid water can be divided into energy saturation and energy dampening phases. The initial increases in Tb are accompanied by the amplification of ε until the liquid water reaches a certain level. The subsequent energy dampening phase is characterized by monotonic decreases in Tb, which are caused by the increase in snow-air interface reflectivity due to the amplified real part of the refractive index (Kang et al., 2014) (Fig. 1).

Tb_{V36} of the fine-grained snowpack increases rapidly in the energy saturation phase with a slight amount of liquid water, and daily Tb variations are large because of the contrasting freeze/thaw state. Therefore, both single-channel and DAV methods can recognize these sharp changes in the early melt season. During the melt seasons, snow grain size can increase to 2 mm when meltwater refreezes in the pore space (Winebrenner et al., 1994). As a result, Tb_{V36} of the coarse-grained snowpack is much lower than that of the fine-grained snowpack due to enhanced volume scattering. Single-channel methods may fail to work when the Tb_{V36} of a melting snowpack is even lower than the winter mean in the late melt season (Zheng et al., 2018). By contrast, significant daily Tb_{V36} variations still exist in the transition from a dry to wet snow regime during the heavy melt season, even when day-time Tb_{V36} is in the energy dampening phase (Fig. 1). Diurnal freeze-thaw cycles are prevalent in polar regions (Hall et al., 2009; Willmes et al., 2009; van den Broeke et al., 2010b). The simulations suggest that the DAV method can detect melt signals for both the melt onset (e.g., Willmes et al., 2009) and the entire melt season when diurnal freeze/thaw transition occurs (e.g., Zheng et al., 2018). Moreover, the optimum acquisition time of AMSR-E/2 enables us to take full advantage of the DAV method in melt detection.

3.2 Melt detection methods

A vertically polarized SSM/I 37 GHz DAV (DAV37) has been used in melt detection on the Greenland ice sheet and Antarctic sea ice (Willmes et al., 2006, 2009; Tedesco, 2007; Arndt et al., 2016). Extensive summer daily freeze-thaw cycles on the Antarctic sea-ice were found by SSM/I (Willmes et al., 2009). AMSR-E/2 have more opportunities to identify these transitions due to the more appropriate local acquisition time. AMSR-E/2 36.5 GHz DAV in vertical polarization (DAV36), were used to detect the pan-Antarctic snowmelt and calculated as follows:

$$DAV36 = | Tb_{V36A} - Tb_{V36D} | \tag{2}$$

where Tb_{V36A} and Tb_{V36D} are the Tb_{V36} in ascending and descending passes respectively. Willmes et al. (2009) determined melt signals when the DAV37 of SSM/I exceeds 10 K. The threshold was validated against extensive field data on the Antarctic sea ice. We utilized the same threshold for melt detection based on AMSR-E/2 DAV36 considering the differences between AMSR-E 36 GHz Tb and SSM/I 37 GHz Tb are very small (Dai and Che, 2010). In the region south of 85° S where the surface snow is stable and never melts, the bias between the two measurements was only approximately 1 K during 2002-2003

(Supplement Fig. 1). Slight Tb offsets between different sensors should not affect the results when using temporal Tb variability in melt detection (Markus et al., 2009).

This method was also applied in the investigation of snow surface freeze/thaw cycles on the AIS. The verification of snowmelt is difficult, especially in the pan-Antarctic where meltwater refreezes quickly, and climatic data are sparse. However, surface snowmelt is determined by atmospheric conditions and agrees well with the Tair distribution pattern (Tedesco, 2007; Liang et al., 2013). In-situ Tair measurements at Zhongshan Station (69.37°S, 76.38°E) obtained from the Chinese National Arctic and Antarctic Data Center (www.chinare.org.cn) were used to evaluate the DAV36 algorithm (Fig. 2). The overall accuracy (p_0, the proportion of observed agreement) and Kappa coefficient $k = (p_0 - p_c)/(1 - p_c)$ were used to measure the coincidence based on the confusion matrix, where p_c is the proportion in agreement due to chance (Cohen, 1960). Tb_{V36A} and Tb_{V36D} showed sharp increases at melt onset, while decreased below the winter mean in the late melt seasons with associated snow metamorphism. However, positive maximum Tair agreed well with melt signals (i.e., the presence of liquid water) determined by the DAV method, with an overall accuracy of 0.93 and a Kappa coefficient of 0.79.

When a snowpack on sea ice begins to melt, it appears as a blackbody at microwave wavelengths and the Tb increases sharply (Markus et al., 2009), while open water exhibits much lower Tb (Markus and Cavalieri, 1998). Therefore, Tb amplitudes may not be strong enough to be identified as melt signals for first-year sea ice with sufficient open water. To eliminate the effect of open water in melt detection, $DAV36_{ice}$ (i.e., DAV36 contributed by the ice-covered portion) was applied in the Antarctic sea ice snowmelt detection. Regardless of the atmospheric effects, the Tb of sea ice is comprised of the ice portion (Tb_{ice}) and open water portion (Tb_{ow}) (Markus and Cavalieri, 1998):

$$Tb = Tb_{ice} \, SIC + Tb_{ow} \, (1-SIC) \tag{3}$$

therefore, $DAV36_{ice}$ can be calculated as follows:

$$DAV36_{ice} = \left| \frac{Tb_{V36A} - Tb_{ow}(1-SIC_A)}{SIC_A} - \frac{Tb_{V36D} - Tb_{ow}(1-SIC_D)}{SIC_D} \right| \tag{4}$$

where SIC_A and SIC_D represent the SIC for ascending and descending passes. If we assume that the SIC of the two passes remains unchanged (i.e., $SIC_A = SIC_D$), then we have:

$$DAV36_{ice} = \frac{\left| Tb_{V36A} - Tb_{V36D} \right|}{SIC} \tag{5}$$

Fig. 3 shows the comparison of meteorological observations of a sea ice buoy in the Weddell Sea and the corresponding AMSR2 measurements. Snow buoy observations (Fig. 3a), including snow depth and Tair, were obtained from the Alfred Wegener Institute (AWI, http://www.meereisportal.de/en/seaicemonitoring/buoy-mapsdata/). The inset map in Fig. 3b illustrates the annual mean SIC and the route of the buoy from multi-year ice to first-year ice in the Weddell Sea. Tb_{V36A} and Tb_{V36D} showed great differences in the melt season. Sporadic melt events were detected before December 2014. Accompanied by a slight decrease of snow depth, DAV36 exceeded 10 K and Tair went above the freezing point after mid-December. $DAV36_{ice}$ was nearly equal to DAV36 when SIC was above 90%, while it was much higher than the latter when the SIC

dropped after February. DAV36 was below 10 K with Tair above the freezing point many times (see the black arrows), while these melt signals were successfully recognized by DAV36$_{ice}$ algorithm. The overall accuracy and Kappa coefficient between the positive maximum Tair and melt signals derived by satellites were 0.79 and 0.51 based on the DAV36 algorithm and 0.82 and 0.60 based on the DAV36$_{ice}$ algorithm. DAV36$_{ice}$ algorithm performs better than DAV36 algorithm in the marginal ice zone by reducing the effect of open water.

To capture complete melt seasons, a melting year begins on 1 July and ends on 30 June of the next year. The missing observations were filled based on time-line interpolation. Spurious Tb variations may occasionally be mistaken for melt signals, which can be caused by clouds, atmospheric water vapor, wind-induced surface roughening, and residual calibration errors. To mitigate their impacts on melt detection, a median filter with a 3×3 window was applied to the satellite observations. Further, melt detection was constrained to the days with compatible thermal regimes following Belchansky et al. (2004). The days with ERA-Interim Tair > -5°C were first determined, and the DAV36 algorithm was applied henceforth.

Considering the existence of both transient and persistent snowmelt in the pan-Antarctic, early melt onset (EMO, the first day when snowmelt is detected) and continuous melt onset (CMO, the first day when snowmelt lasts for at least three consecutive days) were investigated in this study. Melting days was calculated by summing the number of days with snowmelt. Sufficient Antarctic sea ice melts quickly in austral summer and does not emerge again in the melting year. In such cases, the last day of snowmelt is always the day that sea ice disappears, rather than the day that freeze-up begins. Thus freeze-up and melt duration were not included in this study. Antarctic sea ice cover has exhibited considerable regional and annual variations (Hobbs et al., 2016). To be consistent, the melting days fraction (MDF) and melt extent fraction (MEF) were introduced to study the snowmelt variations:

$$MDF= \frac{Melting\ days}{Ice\ cover\ days}, \tag{6}$$

$$MEF= \frac{Melt\ extent}{Ice\ cover\ extent} \tag{7}$$

where ice cover was determined with SIC > 15% for sea ice, and the AIS is assumed to be ice-covered all the year.

Melt signals derived from the DAV method and the positive Tair from AWS were not always strictly connected (Figs. 3&4). Their differences may be attributed to inconsistent temporal resolutions because snowmelt and refreezing can occur at any time of the day. The daily maximum Tair was derived from hourly Tair records, while only two daily satellite observations were used in the DAV method. In addition, snowmelt may occur when Tair is below the freezing point because of the penetration and absorption of solar radiation within the snowpack (Koh and Jordan, 1995). Markus et al. (2009) have determined the Arctic sea ice freeze/thaw states based on gridded Tair data set with a threshold of -1°C. To evaluate the performance of the DAV method on a larger scale, snowmelt over the pan-Antarctic was also determined by ERA-interim reanalysis when the daily maximum Tair exceeded -1°C.

4 Results

4.1 Snowmelt distribution

The study area was divided into six parts to investigate regional discrepancies in surface snowmelt on sea ice and ice sheet according to Parkinson and Cavalieri (2012) (Fig. 4), namely, the Weddell Sea (WS, 60 °W to 20 °E), Indian Ocean (IO, 20 °E to 90 °), Pacific Ocean (PO, 90 °E to 160 °E), Ross Sea (RS, 160 °E to 130 °W), Bellingshausen Amundsen Sea (BAS, 130 °W to 60 °W), and the AIS.

Integrated pan-Antarctic annual melt indices were examined based on AMSR-E/2 (Fig. 5a-d). On average, pan-Antarctic EMO occurred on 24 September (DOY 86), CMO arrived 53 days later (16 November), and snowmelt lasted for 30 days during 2012-2017 (Table 1). In general, snowmelt shows significant latitudinal zonality. EMO and CMO occur later from the marginal sea ice to the inland of the AIS, from low-latitudes to high-latitudes, while MDF increases in the opposite direction. In some parts of the marginal sea ice zone, EMO was later than that in higher altitudes. This is because sea ice did not occur in these regions until early September (Stammerjohn et al., 2008), while transient surface snowmelt can occur before that in August at lower latitudes (Supplement Fig. 2). However, the earliest CMO was still found in the marginal sea ice zone (Fig. 5b,d).

Annual mean EMO, CMO, melting days and MDF of the six regions were also analyzed (Table 1). In terms of the satellite observations, the earliest EMO (15 August) and CMO (5 November) occurred in BAS where surface snow melted for 37 days. As expected, snowmelt on the AIS began the latest with EMO occurring on 7 December and CMO occurring on 18 December. Sea ice surface snow in WS can melt for more than 100 days (Fig. 5c). MDF can reach 30% for the marginal sea ice in RS and WS (Fig. 5d). Snowmelt at high-latitudes was variable. For example, surface snowmelt on the Ross Ice Shelf extended to the inland area and even reached the Transantarctic Mountains in 2004-2005, but the Ross Ice Shelf was almost totally frozen during 2009-2011 (not shown).

The spatial distribution patterns of pan-Antarctic surface snowmelt derived from AMSR-E/2 and ERA generally agreed well with each other, especially for the AIS (Table 1 and Fig. 5). On average, pan-Antarctic EMO and CMO derived by satellites were 12 days and 27 days later than that detected by ERA. AMSR-E/2 detected later EMO on the near-shore sea ice, and later CMO in BAS and RS (Fig. 5i,j). ERA recognized more melt events in WS (16 days), BAS (19 days), and RS (20 days), where intense surface snowmelt was found (Fig. 5k). Satellite-based MDF for the marginal sea ice is lower than that derived by ERA (Fig. 5l). With the exception of the Antarctic Peninsula where the melt season can last for more than three months, the AIS melt timings detected by the two methods were consistent with each other (Fig. 5i-l).

Seasonal evolution of snowmelt in different regions was examined by the normalized histograms of annual mean EMO, CMO, melting days and MDF (Fig. 6). Notable differences existed between the temporal distribution of sea ice and ice sheet melt patterns. Sea ice EMO concentrated in mid-July for BAS, and in early August for IO. By contrast, the frequency of AIS EMO did not reach the peak until early January. The occurrence of pan-Antarctic CMO peaked in December, varying from early December in BAS and WS to late December in the AIS. Melting days and MDF histograms indicate a large number of

transient melt events, especially in the AIS. Approximately16% of the AIS experienced snowmelt over 2002-2017; however, approximately 66% of these areas melted for no more than 5 days. In general, melting days seldom exceeded 45 d, with the exception of the BAS and WS where plenty of surface snow can melt for more than two months. The annual mean MDF in the BAS was 17% (Table 1), while the MDF in most of the AIS was below 5% (Fig. 6).

5  The CMO histogram suggests that most of the pan-Antarctic continuous snowmelt began between October and January (Fig. 6), corresponding to a sharp increase in MEF (Fig. 7). In mid-January, most of the Antarctic sea ice experienced surface snowmelt, and the daily mean MEF can reach 80%. The AIS daily mean MEF was much lower and also reached a maximum (8%) in mid-January (Fig. 7). MEF declined rapidly between late January and March. The Antarctic sea ice daily mean MEF declined to below 10% and the AIS became almost completely refrozen after April.

10 **4.2 Trend analysis**

Trends in surface melting conditions during 2002-2017 were analyzed. Linear trends in the melt indices were calculated based on the annual departures. As listed in Table 2, the pan-Antarctic snowmelt overall showed a significant trend (at the 90% confidence level) towards later EMO (0.68 days yr^{-1}), especially in the RS and BAS. Trends in CMO, melting days and MDF were not statistically significant for the pan-Antarctic. EMO came significantly later (at the 99% confidence level) in RS (1.72

15 days yr^{-1}). Melting days in RS was also significantly decreased (at the 90% confidence level). The largest trend in EMO (2.13 days yr^{-1}) was observed in BAS. CMO occurred significantly earlier in WS and IO where MDF also significantly increased. Melting days and MDF have both significantly increased (above the 95% confidence level) in PO. The AIS showed a negative trend in surface snowmelt with a later EMO and CMO, and slightly decreasing melting days and MDF.

  The inter-annual departures of melt indices for the pan-Antarctic, AIS and RS where the most significant change in EMO

20 was found are shown in Fig. 8. Melt indices showed considerable inter-annual variations. Pan-Antarctic EMO came much later in recent years after reaching the earliest point in 2010-2011. RS and AIS presented negative trends in surface snowmelt, which were indicated by all the melt indices. The earliest EMO in RS was found in 2004-2005 when nearly the entire Ross Ice Shelf experienced snowmelt. All the AIS snowmelt indices indicated the weakest melt season in 2014-2015.

  The considerable decrease in surface snowmelt in the RS can also be clearly seen in Fig. 9, which illustrates the trends in

25 melt indices during 2002-2017. Most of the pan-Antarctic showed a later EMO, especially in RS where melting days also presented remarkable negative trends. Surface snow on the East Antarctic sea ice, especially in PO, presented trends towards a later EMO. However, melting days and MDF in these regions have increased. EMO and CMO appeared earlier on the marginal sea ice in WS where melting days and MDF also significantly increased. Many low-lying ice shelves in the AIS, such as the Larsen C Ice Shelf in the Antarctic Peninsula and the Abbot Ice Shelf in Marie Byrd Land, presented trends towards

30 decreasing melting days and MDF.

5 Discussion

5.1 Comparisons

EMO and CMO derived from ERA were earlier than that detected by AMSR-E/2 data (Fig. 5 and Table 1). This is because it takes time to produce liquid water when snow temperature approaches the melting point (Markus et al., 2009). Daily Tb variation is limited when liquid water does not refreeze or snowpack is still melting in the warm nights during heavy melt seasons (Willmes et al., 2009; Semmens and Ramage, 2014). As a result, ERA recognized more melt events for the regions where heavy snowmelt was found and the DAV method fails to work, such as the WS, BAS, RS and the Larsen C ice shelf. The might also be the reason that the melt onset was very early in RS while few melt events were detected by AMSR-E/2.

Willmes et al. (2009) established the SSM/I DAV method to study the Antarctic sea ice CMO (hereafter W09). Antarctic sea ice CMO mapped by AMSR-E shows a higher spatial continuity than that in W09. CMO derived from the two satellites agreed well with each other at high latitudes during 2002-2008. However, W09 found a remarkably later CMO on the marginal sea ice compared with results from AMSR-E (Fig. 10). There are several reasons for the significant difference in marginal sea ice CMO detected by AMSR-E and SSM/I data. First, W09 only studied surface snowmelt on sea ice after 1 October, while the melt season begins on 1 July in this study. Second, the DAV36$_{ice}$ algorithm can amplify snowmelt signals by reducing the effect of open water, so that more melt events can be recognized (Fig. 3). Third, compared with SSM/I, AMSR-E operated in a stable orbit and observed the pan-Antarctic with more appropriate local acquisition time, and hence had more opportunities to identify melt events (Supplement Fig. 2).

Considering that snowmelt can be biased by various SMMR and SSM/I acquisition times, Picard and Fily (2006) retrieved the AIS surface snowmelt based on corrected 18-19 GHz Tb time series (hereafter PF06). The AIS daily melt extent derived by AMSR-E/2 and ERA were consistent with each other with R^2=0.92. The PF06 daily melt extent also presented a high correlation with results from AMSR-E/2 (R^2=0.77). However, the melt extent derived by PF06 was significantly smaller than that mapped by AMSR-E/2 (Fig. 11a). AMSR-E/2 and ERA daily mean melt extent were more than twice the melt extent mapped by PF06 from December to February (Fig. 11b). During the melt seasons, Tb may decrease due to the strong volume scattering resulting from the snow metamorphism (Ramage and Isacks, 2002; Markus et al., 2009). Summer Tb can even be much lower than the winter observations (Zheng et al., 2018). PF06 determined snowmelt when the SSM/I 19 GHz Tb exceeds the winter mean plus 2.5 times the standard deviation of the winter Tb; therefore, it may underestimate surface snowmelt. Moreover, as explained in Section 3.1 and as shown in Fig. 1, Tb decreases during the energy dampening phase. Single-channel methods such as PF06 may miss the melt signals during a heavy melt season, while the DAV method is unaffected by snow metamorphism and can detect snowmelt even during the energy dampening phase.

5.2 Uncertainties

There are several uncertainties in the pan-Antarctic snowmelt derived from AMSR-E/2 data. First, the DAV method may fail to work when liquid water does not refreeze or snowpack is still melting in warm nights (Willmes et al., 2009). The regions

with snowmelt that became more prevalent would presumably show a decrease in melting days based on the DAV method. Fortunately, unlike the Arctic, surface snowmelt on the Antarctic sea ice is always patchy and relatively short-lived (Drinkwater and Liu, 2000). Second, although the DAV method used in this study performs well when compared with meteorological observations, the optimal threshold may differ temporally and regionally with varying snow properties. In addition, ice disintegrates, brine and flooding effects may play an important role in seasonal and even diurnal sea ice Tb variations, further complicating the story (Smith, 1998; Willmes et al., 2009). Arndt et al. (2016) utilized individual local thresholds with a median value of 6 K to detect snowmelt based on SSM/I DAV and recognized an earlier melt onset than W09. Melt indices derived from the DAV method showed considerable variations when applying different thresholds (from 6 to 14 K in Fig. 12). Varying the threshold applied to AMSR-E/2 DAV by ±4 K results in -17 days to 14 days departure for the annual mean EMO, and -9 days to 12 days departure for annual mean melting days. It should be noted that the presence of snow liquid water detected by AMSR-E/2 does not necessarily mean that the snowpack is melting because it takes time for meltwater to refreeze. In addition, after refreezing of surface snow, subsurface liquid water can still be detected by radiometer due to the penetrating capacity of microwaves (Ashcraft and Long, 2006). The DAV36$_{ice}$ algorithm for sea ice snowmelt detection assumes that the SIC of the two passes remains unchanged, which may not be true and lead to misidentifications of melt signals due to quick sea ice drift and disintegration. The algorithm can be further improved if the twice-daily SIC product is available in the future.

5.3 Response of the pan-Antarctic surface snowmelt to atmospheric indices

Snowmelt in the pan-Antarctic was found to be strongly associated with the atmospheric component of the El-Niño Southern Oscillation (ENSO) and the Southern Annular Mode (SAM) (Turner, 2004; Tedesco and Monaghan, 2009; Oza et al., 2011; Meredith et al., 2017). In January 2016, the extensive surface snowmelt in West Antarctica was likely linked with sustained and strong advection of warm marine air due to the concurrent strong El Nino event (Nicolas et al., 2017). The weakly negative trend in surface temperature in Antarctica was consistent with the positive trends in SAM during summer and autumn since the 1970s (Monaghan et al., 2008).

To study the response of the pan-Antarctic surface snowmelt to atmospheric conditions, we explored the relationship between the melt indices and Nino3.4 (Rayner et al., 2003), Southern Oscillation Index (SOI) (Ropelewski et al., 1987) and SAM (Marshall, 2003) (Table 3). The CMO of the pan-Antarctic was significantly correlated (at the 95% confidence level) with summer (DJF) SAM. CMO and MDF were also well correlated with summer SAM in RS, BAS and AIS. The correlation coefficient between EMO and SAM was the highest (0.77) in IO. CMO was significantly correlated with SOI and Nino3.4 in RS. Melting days and MDF were also found to be strongly correlated with summer SOI or Nino3.4 in BAS where strong decreases in sea-ice concentration and duration were always linked with contemporary ENSO warm events (Kwok et al., 2002; Bromwich et al., 2004).

MDF was negatively related to summer SAM for off-shore sea ice in BAS and RS where MDF has significantly decreased (Fig. 13). This relationship was especially significant in the AIS (R=-0.88, P<0.01). High anti-correlations were found between

summer SAM and the annual mean MEF on the Antarctic sea ice and AIS (Fig. 13b). The significantly decreased (at the 95% confidence level) annual mean melt extent on the AIS (-0.37×10^4 km^2 yr^{-1}) during 2002-2017 was strongly associated with increasing summer SAM (R=-0.82, P<0.01). This phenomenon is in line with the decreased surface snowmelt and the enhanced summer SAM in AIS since the 1970s (Marshall, 2003; Tedesco and Monaghan, 2009). The positive SAM results in

5   anomalously strong westerlies over the Southern Ocean and hence the reduction in poleward heat transport, leading to the subsequent atmospheric cooling in the Antarctic regions (Thompson and Solomon, 2002). SAM is the principal driver of AIS near-surface temperature and snowmelt variability (Marshall, 2007; Tedesco and Monaghan, 2009), and it is expected to have a continuous effect on the Antarctic climate in the next few decades considering the projected ozone recovery (Thompson et al., 2011).

10   **6 Conclusions**

In this study, we investigated the pan-Antarctic surface melting conditions during 2012-2017 by using daily AMSR-E/2 Tb variations. Compared with SSM/I, the more stable orbit and more appropriate local acquisition time of AMSR-E/2 enable us to take full advantage of the DAV method to investigate surface melt events. The performance of this method was improved in the marginal sea ice zone by excluding the effect of open water. Although the DAV method may fail to recognize melt

15   events when meltwater does not refreeze or snowpack melts in the warm nights, snowmelt detected by AMSR-E/2 agreed well with the positive Tair observations, and was more extensive than that detected by SSM/I.

    Pan-Antarctic snowmelt showed significant latitudinal zonality. On average, early snowmelt begins in late September, while continuous snowmelt begins in mid-November. Sea ice in WS can melt for more than 100 days. Snowmelt on the Antarctic sea ice and AIS exhibited great differences in temporal distribution patterns. The pan-Antarctic showed a significant

20   trend (at the 90% confidence level) towards later EMO (0.68 days yr^{-1}). Negative trends in snowmelt were found in RS and AIS. CMO in the pan-Antarctic was well correlated with summer SAM. The decreasing surface snowmelt in the AIS was very likely linked with the positive summer SAM trend during 2002-2017.

    Though AMSR-E/2 observed the pan-Antarctic at the appropriate time for snowmelt detection, they may underestimate snowmelt because snowmelt can occur at any time and refreezing can be quasi-instantaneous. Other sources of the microwave

25   remote sensing data set, such as scatterometer and synthetic aperture radar, are expected to enrich daily observations in future works. Snowmelt derived by satellites can serve as input and output validations for climate models.

Data availability

The AMSR-E and AMSR2 data were obtained from the National Snow and Ice Data Center (NSIDC) and the Japan Aerospace Exploration Agency (JAXA). Sea ice concentration data was also provided by NSIDC. The ERA-Interim is available from the European Centre for Medium-Range Weather Forecasts (ECMWF).

5 **Competing interests**

The authors declare that they have no conflict of interest.

Acknowledgements

We would like to express our gratitude to the editor and reviewers for their careful and insightful comments. The numerical calculations in this paper have been done on the supercomputing system in the Supercomputing Center of Wuhan University.
10 This research was funded by the National Natural Science Foundation of China (NSFC) (Grant nos. 41376187, 41531069 and 41776200).

References

Abdalati, W. and Steffen, K.: Passive microwave-derived snow melt regions on the Greenland Ice Sheet, Geophys. Res. Lett., 22(7), 787–790, doi:10.1029/95GL00433, 1995.

15 Ackley, S. F., Lewis, M. J., Fritsen, C. H. and Xie, H.: Internal melting in Antarctic sea ice: Development of "gap layers," Geophys. Res. Lett., 35, L11503, doi:10.1029/2008GL033644, 2008.

Arndt, S., Willmes, S., Dierking, W. and Nicolaus, M.: Timing and regional patterns of snowmelt on Antarctic sea ice from passive microwave satellite observations, J. Geophys. Res. Ocean., 121(8), 5916–5930, doi:10.1002/2015JC011504, 2016.

20 Ashcraft, I. S. and Long, D. G.: Comparison of methods for melt detection over Greenland using active and passive microwave measurements, Int. J. Remote Sens., 27(12), 2469–2488, doi:10.1080/01431160500534465, 2006.

Belchansky, G. I., Douglas, D. C. and Platonov, N. G.: Duration of the Arctic sea ice melt season: Regional and interannual variability, 1979-2001, J. Clim., 17(1), 67–80, doi:10.1175/1520-0442(2004)017<0067:DOTASI>2.0.CO;2, 2004.

Bell, R. E., Banwell, A. F., Trusel, L. D. and Kingslake, J.: Antarctic surface hydrology and impacts on ice-sheet mass balance,
25 Nat. Clim. Chang., 8(12), 1044–1052, doi:10.1038/s41558-018-0326-3, 2018.

Bliss, A., Miller, J. and Meier, W.: Comparison of Passive Microwave-Derived Early Melt Onset Records on Arctic Sea Ice, Remote Sens., 9(3), 199, doi:10.3390/rs9030199, 2017.

Brandt, R. E., Warren, S. G., Worby, A. P. and Grenfell, T. C.: Surface albedo of the Antarctic sea ice zone, J. Clim., 18(17),

3606–3622, doi:10.1175/JCLI3489.1, 2005.

Bromwich, D. H., Monaghan, A. J. and Guo, Z.: Modeling the ENSO modulation of Antarctic climate in the late 1990s with the Polar MM5, J. Clim., 17(1), 109–132, doi:10.1175/1520-0442(2004)017<0109:MTEMOA>2.0.CO;2, 2004.

Brucker, L., Picard, G. and Fily, M.: Snow grain-size profiles deduced from microwave snow emissivities in Antarctica, J.
5   Glaciol., 56(197), 514–526, doi:10.3189/002214310792447806, 2010.

Cohen, J.: A Coefficient of Agreement for Nominal Scales, Educ. Psychol. Meas., 20(1), 37–46, doi:10.1177/001316446002000104, 1960.

Comiso, J.: Bootstrap Sea Ice Concentrations from Nimbus-7 SMMR and DMSP SSM/I-SSMIS, Version 3. NASA National Snow and Ice Data Center Distributed Active Archive Center, NSIDC, doi:10.5067/7Q8HCCWS4I0R, 2017.

10   Comiso, J. C. and Nishio, F.: Trends in the sea ice cover using enhanced and compatible AMSR-E, SSM/I, and SMMR data, J. Geophys. Res., 113, C02S07, doi:10.1029/2007JC004257, 2008.

Dai, L. and Che, T.: Cross-platform calibration of SMMR, SSM/I and AMSR-E passive microwave brightness temperature, Sixth Int. Symp. Digit. Earth Data Process. Appl., 7841, 784103, doi:10.1117/12.873150, 2010.

Dee, D. P., Uppala, S. M., Simmons, A. J., Berrisford, P., Poli, P., Kobayashi, S., Andrae, U., Balmaseda, M. A., Balsamo, G.,
15   Bauer, P., Bechtold, P., Beljaars, A. C. M., van de Berg, L., Bidlot, J., Bormann, N., Delsol, C., Dragani, R., Fuentes, M., Geer, A. J., Haimberger, L., Healy, S. B., Hersbach, H., Hólm, E. V., Isaksen, L., Kållberg, P., Köhler, M., Matricardi, M., McNally, A. P., Monge-Sanz, B. M., Morcrette, J.-J., Park, B.-K., Peubey, C., de Rosnay, P., Tavolato, C., Thépaut, J.-N. and Vitart, F.: The ERA-Interim reanalysis: configuration and performance of the data assimilation system, Q. J. R. Meteorol. Soc., 137(656), 553–597, doi:10.1002/qj.828, 2011.

20   Drinkwater, M. R. and Liu, X.: Seasonal to interannual variability in Antarctic sea-ice surface melt, IEEE Trans. Geosci. Remote Sens., 38(4), 1827–1842, doi:10.1109/36.851767, 2000.

Hall, D. K., Nghiem, S. V., Schaaf, C. B., DiGirolamo, N. E. and Neumann, G.: Evaluation of surface and near-surface melt characteristics on the Greenland ice sheet using MODIS and QuikSCAT data, J. Geophys. Res. Earth Surf., 114, F04006, doi:10.1029/2009JF001287, 2009.

25   Hobbs, W. R., Massom, R., Stammerjohn, S., Reid, P., Williams, G. and Meier, W.: A review of recent changes in Southern Ocean sea ice, their drivers and forcings, Glob. Planet. Change, 143, 228–250, doi:10.1016/J.GLOPLACHA.2016.06.008, 2016.

Intergovernmental Panel on Climate Change (IPCC): Climate change 2013: the physical science basis. Fifth assessment report of the intergovernmental panel on climate change, 2014.

30   Joshi, M., Merry, C. J., Jezek, K. C. and Bolzan, J. F.: An edge detection technique to estimate melt duration, season and melt extent on the Greenland Ice Sheet using Passive Microwave Data, Geophys. Res. Lett., 28(18), 3497–3500, doi:10.1029/2000gl012503, 2001.

Kang, D. H., Barros, A. P. and Dery, S. J.: Evaluating Passive Microwave Radiometry for the Dynamical Transition From Dry to Wet Snowpacks, IEEE Trans. Geosci. Remote Sens., 52(1), 3–15, 2014.

Knowles, M., Armstrong, R. and Brodzik, M. J.: AMSR-E/Aqua Daily EASE-Grid Brightness Temperatures, Version 1. Boulder, Colorado USA. NASA National Snow and Ice Data Center Distributed Active Archive Center, NSIDC, doi:https://doi.org/10.5067/RRR4WWORG070, 2006.

Koh, G. and Jordan, R.: Sub-surface melting in a seasonal snow cover, J. Glaciol., 41(139), 474–482, doi:10.3189/S002214300003481X, 1995.

Kwok, R., Comiso, J. C., Kwok, R. and Comiso, J. C.: Southern Ocean Climate and Sea Ice Anomalies Associated with the Southern Oscillation, J. Clim., 15(5), 487–501, doi:10.1175/1520-0442(2002)015<0487:SOCASI>2.0.CO;2, 2002.

Liang, L., Guo, H., Li, X. and Cheng, X.: Automated ice-sheet snowmelt detection using microwave radiometer measurements, Polar Res., 32(1), 1–13, doi:10.3402/polar.v32i0.19746, 2013.

Liu, H., Wang, L. and Jezek, K. C.: Wavelet-transform based edge detection approach to derivation of snowmelt onset, end and duration from satellite passive microwave measurements, Int. J. Remote Sens., 26(21), 4639–4660, doi:10.1080/01431160500213342, 2005.

Markus, T. and Cavalieri, D. J.: Snow Depth Distribution Over Sea Ice in the Southern Ocean from Satellite Passive Microwave Data, in Antarctic Sea Ice: Physical Processes, Interactions and Variability, vol. 74, pp. 19–39., 1998.

Markus, T., Stroeve, J. C. and Miller, J.: Recent changes in Arctic sea ice melt onset, freezeup, and melt season length, J. Geophys. Res. Ocean., 114, C12024, doi:10.1029/2009JC005436, 2009.

Marshall, G. J.: Trends in the Southern Annular Mode from observations and reanalyses, J. Clim., 16(24), 4134–4143, doi:10.1175/1520-0442(2003)016<4134:TITSAM>2.0.CO;2, 2003.

Marshall, G. J.: Half-century seasonal relationships between the Southern Annular Mode and Antarctic temperatures, Int. J. Climatol., 27(3), 373–383, doi:10.1002/joc.1407, 2007.

Matear, R. J., O'Kane, T. J., Risbey, J. S. and Chamberlain, M.: Sources of heterogeneous variability and trends in Antarctic sea-ice, Nat. Commun., 6, 8656, doi:10.1038/ncomms9656, 2015.

Meier, W. N. and Stroeve, J.: Comparison of sea-ice extent and ice-edge location estimates from passive microwave and enhanced-resolution scatterometer data, Ann. Glaciol., 48, 65–70, doi:10.3189/172756408784700743, 2008.

Meredith, M. P., Stammerjohn, S. E., Venables, H. J., Ducklow, H. W., Martinson, D. G., Iannuzzi, R. A., Leng, M. J., van Wessem, J. M., Reijmer, C. H. and Barrand, N. E.: Changing distributions of sea ice melt and meteoric water west of the Antarctic Peninsula, Deep Sea Res. Part 2. Top. Stud. Oceanogr., 139, 40–57, doi:10.1016/j.dsr2.2016.04.019, 2017.

Monaghan, A. J., Bromwich, D. H., Chapman, W. and Comiso, J. C.: Recent variability and trends of Antarctic near-surface temperature, J. Geophys. Res. Atmos., 113, D04105, doi:10.1029/2007JD009094, 2008.

Mote, T. L. and Anderson, M. R.: Variations in snowpack melt on the Greenland ice sheet based on passive-microwave measurements, J. Glaciol., 41(137), 51–60, 1995.

Nicolas, J. P., Vogelmann, A. M., Scott, R. C., Wilson, A. B., Cadeddu, M. P., Bromwich, D. H., Verlinde, J., Lubin, D., Russell, L. M., Jenkinson, C., Powers, H. H., Ryczek, M., Stone, G. and Wille, J. D.: January 2016 extensive summer melt in West Antarctica favoured by strong El Niño, Nat. Commun., 8, 15799, doi:10.1038/ncomms15799, 2017.

Oza, S. R., Singh, R. K. K., Vyas, N. K. and Sarkar, A.: Study of inter-annual variations in surface melting over Amery Ice Shelf, East Antarctica, using space-borne scatterometer data, J. Earth Syst. Sci., 120(2), 329–336, 2011.

Parkinson, C. L. and Cavalieri, D. J.: Antarctic sea ice variability and trends, 1979–2010, Cryosph., 6, 871–880, doi:10.5194/tc-6-871-2012, 2012.

Picard, G. and Fily, M.: Surface melting observations in Antarctica by microwave radiometers: Correcting 26-year time series from changes in acquisition hours, Remote Sens. Environ., 104(3), 325–336, 2006.

Picard, G., Fily, M. and Gallee, H.: Surface melting derived from microwave radiometers: A climatic indicator in Antarctica, Ann. Glaciol., 46, 29–34, doi:10.3189/172756407782871684, 2007.

Powell, D. C., Markus, T., Cavalieri, D. J. and Gasiewski, A. J.: Microwave Signatures of Snow on Sea Ice: Modeling, IEEE Trans. Geosci. Remote Sens., 44(11), 3091–3102, 2006.

Ramage, J. M. and Isacks, B. L.: Determination of melt-onset and refreeze timing on southeast Alaskan icefields using SSM/I diurnal amplitude variations, Ann. Glaciol., 34, 391–398, doi:10.3189/172756402781817761, 2002.

Ramage, J. M. and Isacks, B. L.: Interannual variations of snowmelt and refreeze timing on southeast-Alaskan icefields, U.S.A., J. Glaciol., 49(164), 102–116, doi:10.3189/172756503781830908, 2003.

Rayner, N. A., Parker, D. E., Horton, E. B., Folland, C. K., Alexander, L. V., Rowell, D. P., Kent, E. C. and Kaplan, A.: Global analyses of sea surface temperature, sea ice, and night marine air temperature since the late nineteenth century, J. Geophys. Res., 108(D14), 4407, doi:10.1029/2002JD002670, 2003.

Ridley, J.: Surface melting on Antarctic Peninsula ice shelves detected by passive microwave sensors, Geophys. Res. Lett., 20(23), 2639–2642, doi:10.1029/93GL02611, 1993.

Ropelewski, C. F., Jones, P. D., Ropelewski, C. F. and Jones, P. D.: An Extension of the Tahiti–Darwin Southern Oscillation Index, Mon. Weather Rev., 115(9), 2161–2165, doi:10.1175/1520-0493(1987)115<2161:AEOTTS>2.0.CO;2, 1987.

Scambos, T., Hulbe, C., Fahnestock, M. and Bohlander, J.: The link between climate warning and break-up of ice shelves in the Antarctic Peninsula, J. Glaciol., 46(154), 516–530, doi:10.3189/172756500781833043, 2000.

Scott, R. C., Nicolas, J. P., Bromwich, D. H., Norris, J. R. and Lubin, D.: Meteorological Drivers and Large-Scale Climate Forcing of West Antarctic Surface Melt, J. Clim., 32(3), 665–684, doi:10.1175/JCLI-D-18-0233.1, 2018.

Semmens, K. and Ramage, J.: Melt patterns and dynamics in Alaska and Patagonia derived from passive microwave brightness temperatures., Remote Sens., 6(1), 603–620, doi:10.3390/rs6010603, 2014.

Serreze, M. G., Maslanik, J. A., Scharfen, G. R., Barry, R. G. and Robinson, D. A.: Interannual variations in snow melt over Arctic sea ice and relationships to atmospheric forcings, Ann. Glaciol., 17, 327–331, doi:10.3189/S0260305500013057, 1993.

Smith, D. M.: Observation of perennial Arctic sea ice melt and freeze-up using passive microwave data, J. Geophys. Res. Ocean., 103(C12), 27753–27769, doi:10.1029/98JC02416, 1998.

Stammerjohn, S. E., Martinson, D. G., Smith, R. C., Yuan, X. and Rind, D.: Trends in Antarctic annual sea ice retreat and advance and their relation to El Niño–Southern Oscillation and Southern Annular Mode variability, J. Geophys. Res., 113,

C03S90, doi:10.1029/2007JC004269, 2008.

Steffen, K.: Surface energy exchange at the equilibrium line on the Greenland ice sheet during onset of melt, Ann. Glaciol., 21, 13–18, 1995.

Stroeve, J. C., Markus, T., Boisvert, L., Miller, J. and Barrett, A.: Changes in Arctic melt season and implifications for sea ice
5   loss, Geophys. Res. Lett., 41, 1216–1225, doi:10.1002/2013GL058951.Received, 2014.

Stroeve, J. C., Mioduszewski, J. R., Rennermalm, A., Boisvert, L. N., Tedesco, M. and Robinson, D.: Investigating the Local Scale Influence of Sea Ice on Greenland Surface Melt, Cryosph., 11, 2363–2381, doi:10.5194/tc-2017-65, 2017.

Sundal, A. V., Shepherd, A., Nienow, P., Hanna, E., Palmer, S. and Huybrechts, P.: Melt-induced speed-up of Greenland ice sheet offset by efficient subglacial drainage, Nature, 469(7331), 521–524, doi:10.1038/nature09740, 2011.

10   Tanaka, Y., Tateyama, K., Kameda, T. and Hutchings, J. K.: Estimation of melt pond fraction over high-concentration Arctic sea ice using AMSR-E passive microwave data, J. Geophys. Res. Ocean., 121(9), 7056–7072, doi:10.1002/2016JC011876, 2016.

Tedesco, M.: Snowmelt detection over the Greenland ice sheet from SSM/I brightness temperature daily variations, Geophys. Res. Lett., 34, L02504, doi:10.1029/2006GL028466, 2007.

15   Tedesco, M.: Assessment and development of snowmelt retrieval algorithms over Antarctica from K-band spaceborne brightness temperature (1979-2008), Remote Sens. Environ., 113(5), 979–997, doi:10.1016/j.rse.2009.01.009, 2009.

Tedesco, M. and Monaghan, A. J.: An updated Antarctic melt record through 2009 and its linkages to high-latitude and tropical climate variability, Geophys. Res. Lett., 36, L18502, doi:10.1029/2009GL039186, 2009.

Tedesco, M., Abdalati, W. and Zwally, H. J.: Persistent surface snowmelt over Antarctica (1987–2006) from 19.35 GHz
20   brightness temperatures, Geophys. Res. Lett., 34, L18504, doi:10.1029/2007gl031199, 2007.

The IMBIE team: Mass balance of the Antarctic Ice Sheet from 1992 to 2017, Nature, 558(7709), 219–222, doi:10.1038/s41586-018-0179-y, 2018.

Thompson, D. W. J. and Solomon, S.: Interpretation of recent Southern Hemisphere climate change, Science, 296(5569), 895–899, doi:10.1126/science.1069270, 2002.

25   Thompson, D. W. J., Solomon, S., Kushner, P. J., England, M. H., Grise, K. M. and Karoly, D. J.: Signatures of the Antarctic ozone hole in Southern Hemisphere surface climate change, Nat. Geosci., 4(11), 741–749, doi:10.1038/ngeo1296, 2011.

Turner, J.: The El Niño-Southern Oscillation and Antarctica, Int. J. Climatol., 24(1), 1–31, doi:10.1002/joc.965, 2004.

van den Broeke, M.: Strong surface melting preceded collapse of Antarctic Peninsula ice shelf, Geophys. Res. Lett., 32, L12815, doi:10.1029/2005GL023247, 2005.

30   van den Broeke, M., Bamber, J., Ettema, J., Rignot, E., Schrama, E., van de Berg, W., van Meijgaard, E., Velicogna, I. and Bert, W.: Partitioning recent Greenland mass loss, Science, 326(5955), 984–986, doi:10.1126/science.1178176, 2009.

van den Broeke, M., König-Langlo, G., Picard, G., Kuipers Munneke, P. and Lenaerts, J.: Surface energy balance, melt and sublimation at Neumayer Station, East Antarctica, Antarct. Sci., 22(1), 87–96, doi:10.1017/S0954102009990538, 2010a.

van den Broeke, M., Bus, C., Ettema, J. and Smeets, P.: Temperature thresholds for degree-day modelling of Greenland ice

sheet melt rates, Geophys. Res. Lett., 37, L18501, doi:10.1029/2010GL044123, 2010b.

Wang, L., Toose, P., Brown, R. and Derksen, C.: Frequency and distribution of winter melt events from passive microwave satellite data in the pan-Arctic, Cryosph., 10, 2589–2602, doi:10.5194/tc-10-2589-2016, 2016.

Wiesmann, A. and Mätzler, C.: Microwave emission model of layered snowpacks, Remote Sens. Environ., 70(3), 307–316, doi:10.1016/S0034-4257(99)00046-2, 1999.

Willmes, S., Bareiss, J., Haas, C. and Nicolaus, M.: The importance of diurnal processes for the Seasonal cycle of Sea-ice microwave brightness temperatures during early Summer in the Weddell Sea, Antarctica, Ann. Glaciol., 44, 297–302, doi:10.3189/172756406781811817, 2006.

Willmes, S., Haas, C., Nicolaus, M. and Bareiss, J.: Satellite microwave observations of the interannual variability of snowmelt on sea ice in the Southern Ocean, J. Geophys. Res., 114, C03006, doi:10.1029/2008JC004919, 2009.

Winebrenner, D. P., Nelson, E. D., Colony, R. and West, R. D.: Observation of melt onset on multiyear Arctic sea ice using the ERS 1 synthetic aperture radar, J. Geophys. Res., 99(C11), 22425–22441, doi:10.1029/94JC01268, 1994.

Zheng, L., Zhou, C., Liu, R. and Sun, Q.: Antarctic Snowmelt Detected by Diurnal Variations of AMSR-E Brightness Temperature, Remote Sens., 10(9), 1391, doi:10.3390/rs10091391, 2018.

Zheng, L., Zhou, C. and Liang, Q.: Variations in Antarctic Peninsula snow liquid water during 1999–2017 revealed by merging radiometer, scatterometer and model estimations, Remote Sens. Environ., 232, 111219, doi:10.1016/j.rse.2019.111219, 2019.

Zwally, H. J.: Microwave Emissivity and Accumulation Rate of Polar Firn, J. Glaciol., 18(79), 195–215, doi:10.3189/S0022143000021304, 1977.

Zwally, H. J. and Fiegles, S.: Extent and duration of Antarctic surface melting, J. Glaciol., 40(136), 463–475, doi:10.1017/S0022143000012338, 1994.

Zwally, H. J., Abdalati, W., Herring, T., Larson, K., Saba, J. and Steffen, K.: Surface Melt-Induced Acceleration of Greenland Ice-Sheet Flow, Science, 297(5579), 218–222, doi:10.1126/science.1072708, 2002.

Table 1. Annual mean and standard deviation of pan-Antarctic EMO, CMO, melting days and MDF derived by AMSR-E/2 and ERA.

Observation	Melt index	WS	IO	PO	RS	BAS	AIS	All
AMSR-E/2	EMO (DOY)	24 Sep (86)±8	22 Sep (84)±6	4 Sep (66)±10	11 Sep (73)±8	15 Aug (46) ±15	7 Dec (160)±6	24 Sep (86)±5
	CMO (DOY)	12 Nov (135)±7	19 Nov (142)±5	15 Nov (138)±6	14 Nov (137)±10	5 Nov (128) ±12	18 Dec (171)±3	16 Nov (139)±4
	Melting days (days)	34±3	21±4	34±4	30±4	37±4	25±3	30±2
	MDF (%)	15±1	11±1	14±1	13±1	17±1	7±1	13±1

ERA	EMO (DOY)	9 Sep (71)±11	16 Sep (78)±16	25 Aug (56)±14	23 Aug (54)±9	28 Jul (28) ±10	3 Dec (156)±5	12 Sep (74)±6
	CMO (DOY)	22 Oct (114)±11	9 Nov (132)±10	22 Oct (114)±12	29 Sep (91)±10	7 Sep (69) ±16	10 Dec (163)±6	20 Oct (112)±7
	Melting days (days)	49±3	26±4	41±5	50±3	56±6	26±2	42±2
	MDF (%)	21±1	13±2	16±2	22±2	26±2	7±1	18±1

Table 2. Trends in pan-Antarctic EMO, CMO, melting days and MDF during 2002-2017. Trends with *, ** and *** indicate statistical significance at 90%, 95%, and 99% confidence levels, respectively. The uncertainties of the trends were estimated at 90% confidence level.

Melt index	WS	IO	PO	RS	BAS	AIS	All
EMO (days yr^{-1})	-0.35±1.10	0.09±0.82	1.37±1.40	1.72±0.71***	2.13±1.88*	0.71±0.76	0.68±0.59*
CMO (days yr^{-1})	-0.82±0.72*	-0.84±0.51**	-0.16±0.71	0.52±1.23	0.59±1.74	0.22±0.51	-0.22±0.43
Melting days (days yr^{-1})	0.34±0.33*	0.37±0.42	0.80±0.46***	-0.52±0.43*	-0.05±0.57	-0.33±0.41	0.11±0.20
MDF (% yr^{-1})	0.20±0.14**	0.15±0.14*	0.19±0.12**	-0.14±0.14	0.02±0.19	-0.09±0.11	0.07±0.08

Table 3. Correlation between snowmelt index and atmospheric index for the Period 2002–2017. Correlation coefficients with *, ** and *** indicate statistical significance at 90%, 95%, and 99% confidence levels, respectively.

Atmospheric index	Melt index	WS	IO	PO	RS	BAS	AIS	All
SAM	EMO	-0.27	0.77***	0.32	0.16	0.25	0.52*	0.31
	CMO	-0.03	0.15	0.03	0.50*	0.53*	0.80***	0.54**
	Melting days	0.37	0.18	0.01	-0.26	-0.42	-0.88***	-0.02
	MDF	0.18	-0.11	-0.07	-0.48*	-0.53*	-0.88***	-0.33
SOI	EMO	0.11	-0.08	-0.01	0.10	0.28	0.55**	0.19
	CMO	0.09	-0.23	0.14	-0.53*	-0.12	0.18	-0.31
	Melting days	0.03	-0.26	0.07	-0.11	0.46*	-0.03	-0.07
	MDF	-0.16	-0.18	0.12	0.15	0.34	-0.03	-0.09
Nino3.4	EMO	-0.28	-0.06	-0.11	-0.02	-0.26	-0.47*	-0.27
	CMO	-0.15	0.19	-0.35	0.66**	0.28	0.01	0.35
	Melting days	0.04	0.42	-0.16	0.08	-0.54**	-0.15	-0.07
	MDF	0.24	0.36	-0.11	-0.22	-0.46*	-0.15	0.13
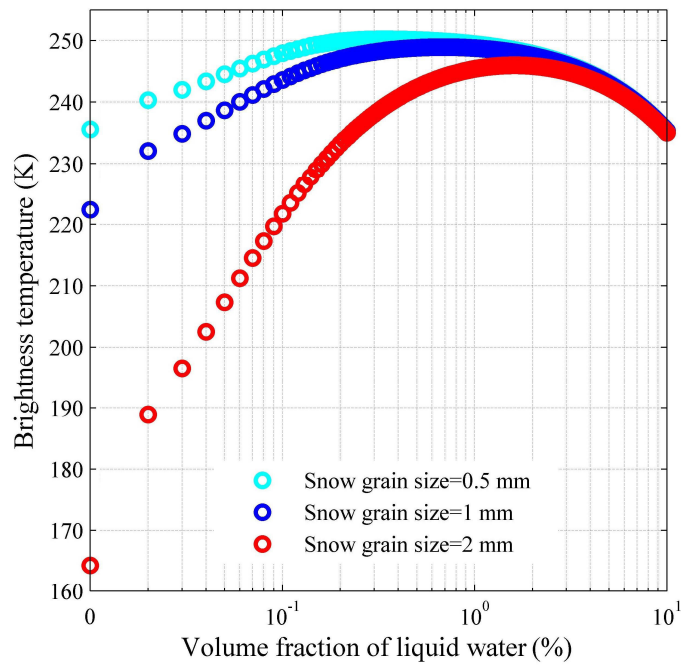
Figure 1. Simulated Tb$_{V36}$ varying with liquid water when the snow grain size is 0.5 cm (cyan), 1 mm (blue) and 2 mm (red).
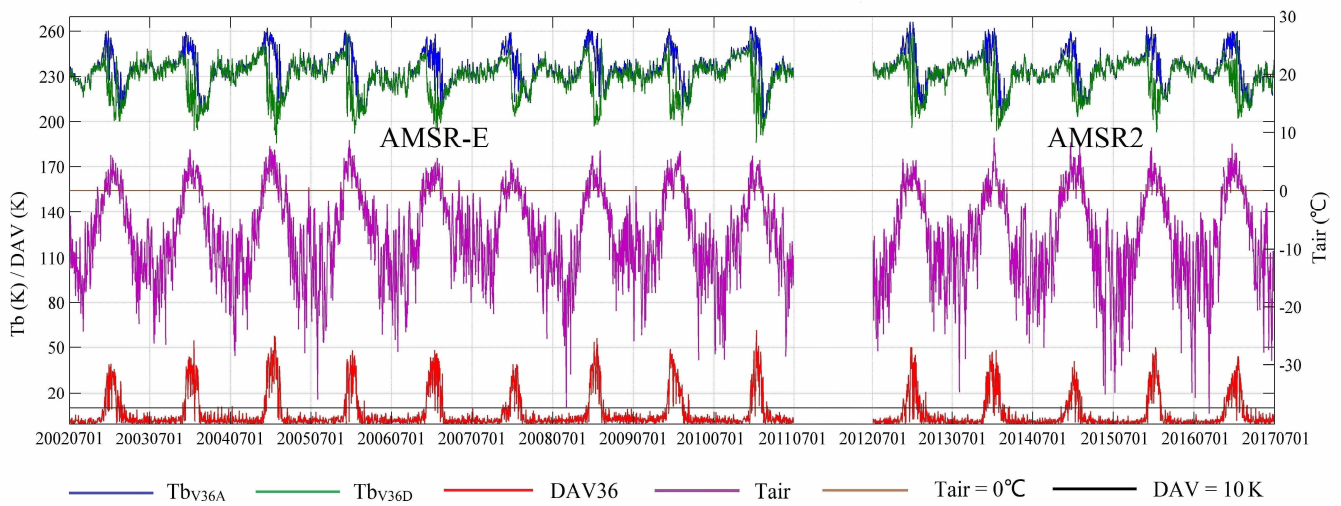
5 **Figure 2. The comparison between Tair and satellite observations (AMSR-E from 2002 to 2011 and AMSR2 from 2012 to 2017) at Zhongshan Station, including daily maximum Tair (purple line), Tb$_{V36A}$ (dark blue line), Tb$_{V36D}$ (dark green line) and DAV36 (red line); Brown and black lines represent Tair = 0℃ and DAV = 10 K.**
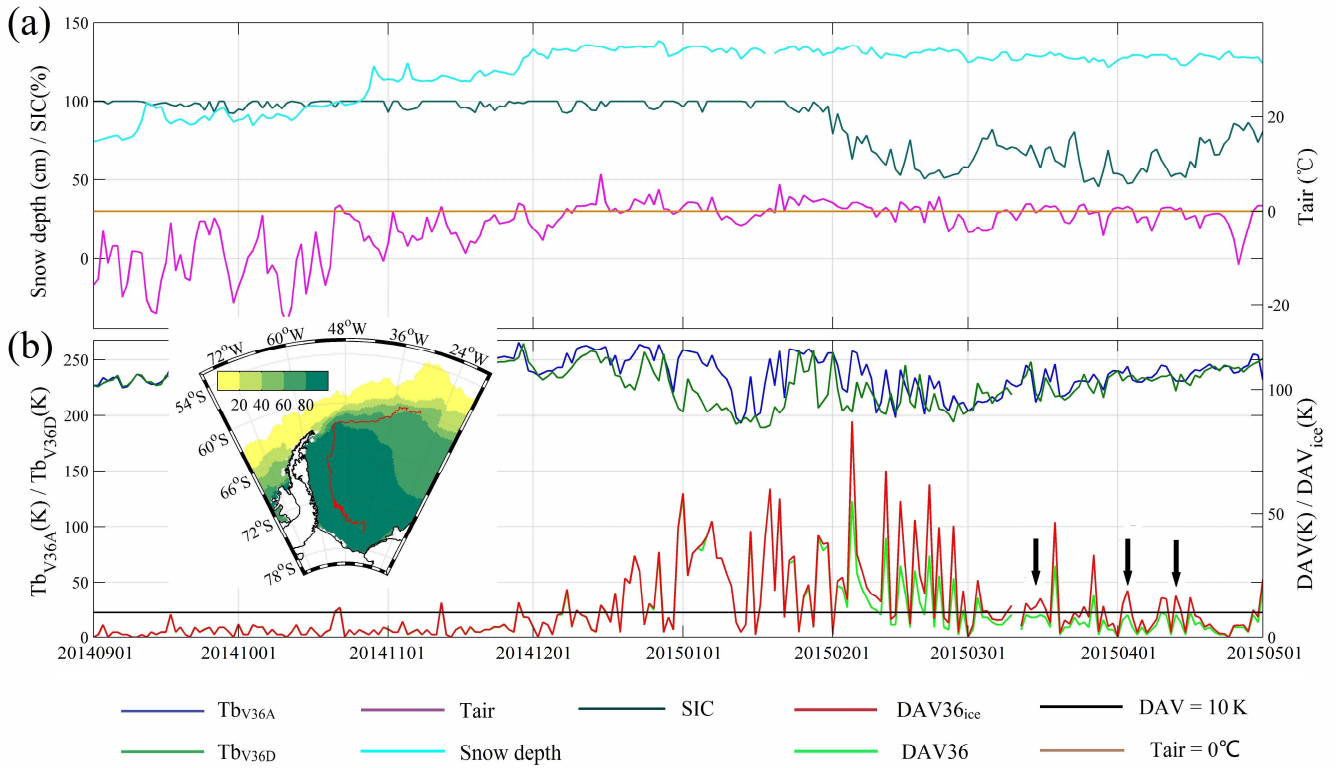
Figure 3. Meteorological and satellite measurements along a sea ice buoy in the Weddell Sea from 1 September, 2014 to 1 May, 2015.
(a) Snow depth (cyan line), daily maximum Tair (pink line), and SIC (olive line); the brown line represents Tair = 0°C. (b) Tb_{V36A}
(dark blue line), Tb_{V36D} (dark green line), DAV36 (light green line) and DAV36$_{ice}$ (red line); the black line represents DAV=10 K.
The inset map in (b) illustrates the annual mean SIC and the route of the buoy from multi-year ice to first-year ice. The black arrows
indicate the cases that melt events were recognized by DAV36$_{ice}$ rather than DAV36.
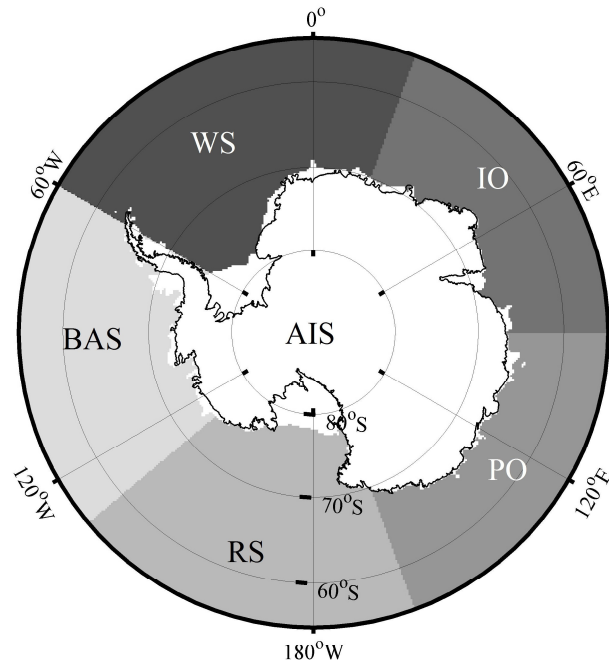
WS-*Weddell Sea*   **IO**-*Indian Ocean*   **PO**-*Pacific Ocean*   **RS**-*Ross Sea*

BAS-*Bellingshausen Amundsen Sea*   **AIS**-*Antarctic ice sheet*

Figure 4. Map of the different regions across the pan-Antarctic.
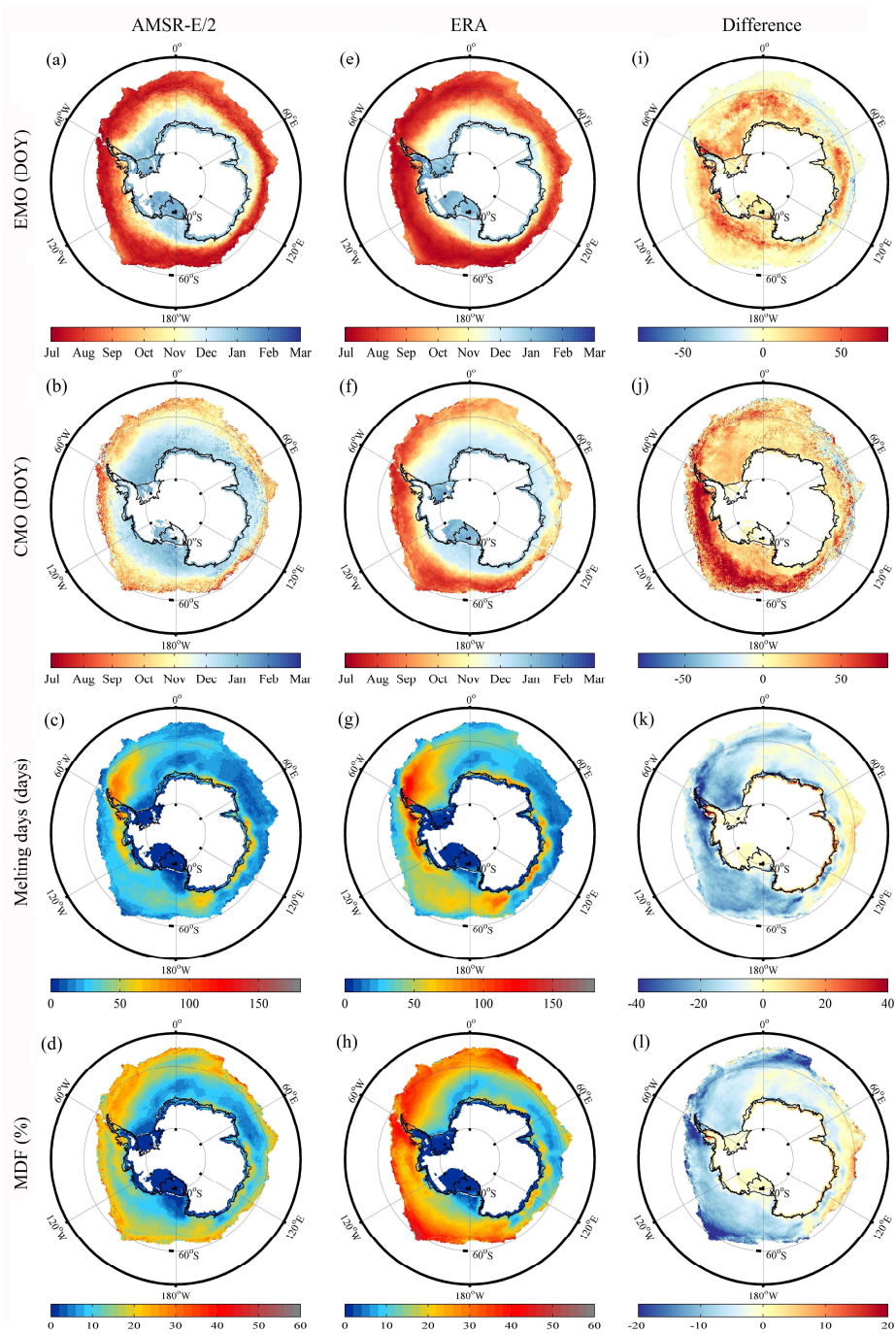
Figure 5. Annual mean EMO, CMO, melting days and MDF derived by AMSR-E/2 (a-d) and ERA (e-h), also shown are the differences (AMSR-E/2 minus ERA) between the two observations (i-l).
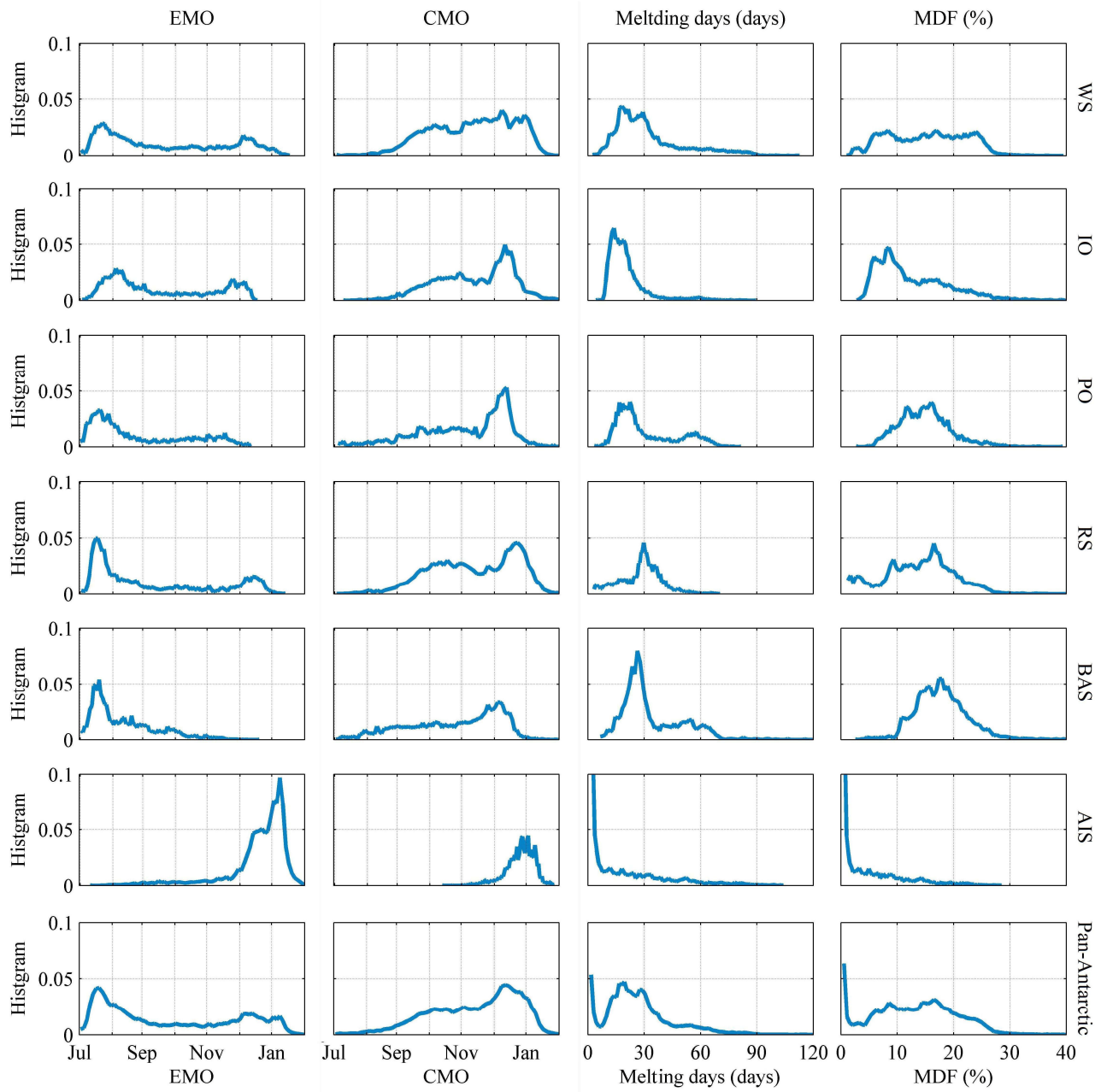
Figure 6. Normalized histograms of annual mean EMO, CMO, melting days and MDF for pan-Antarctic and different regions.
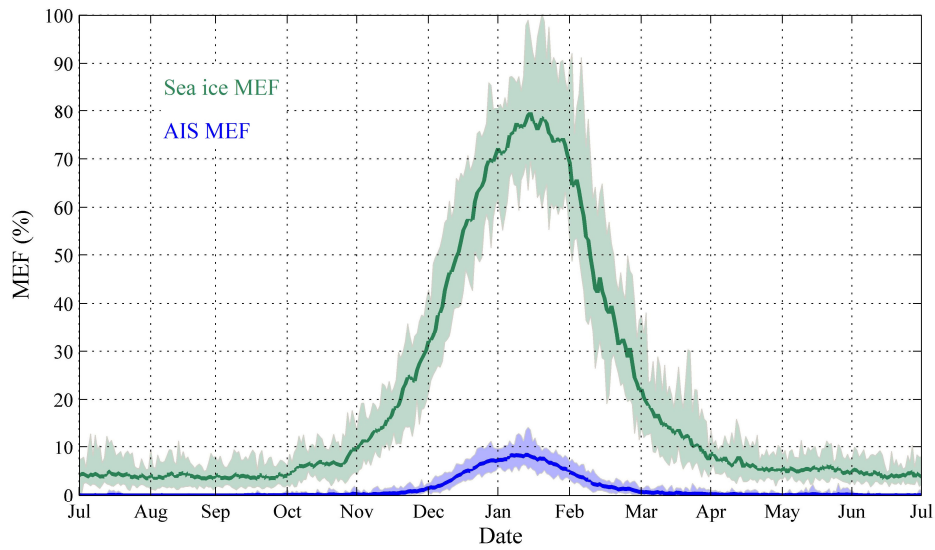
Figure 7. Daily mean Antarctic sea ice MEF and AIS MEF, the corresponding shadows indicate daily maximums and minimums.
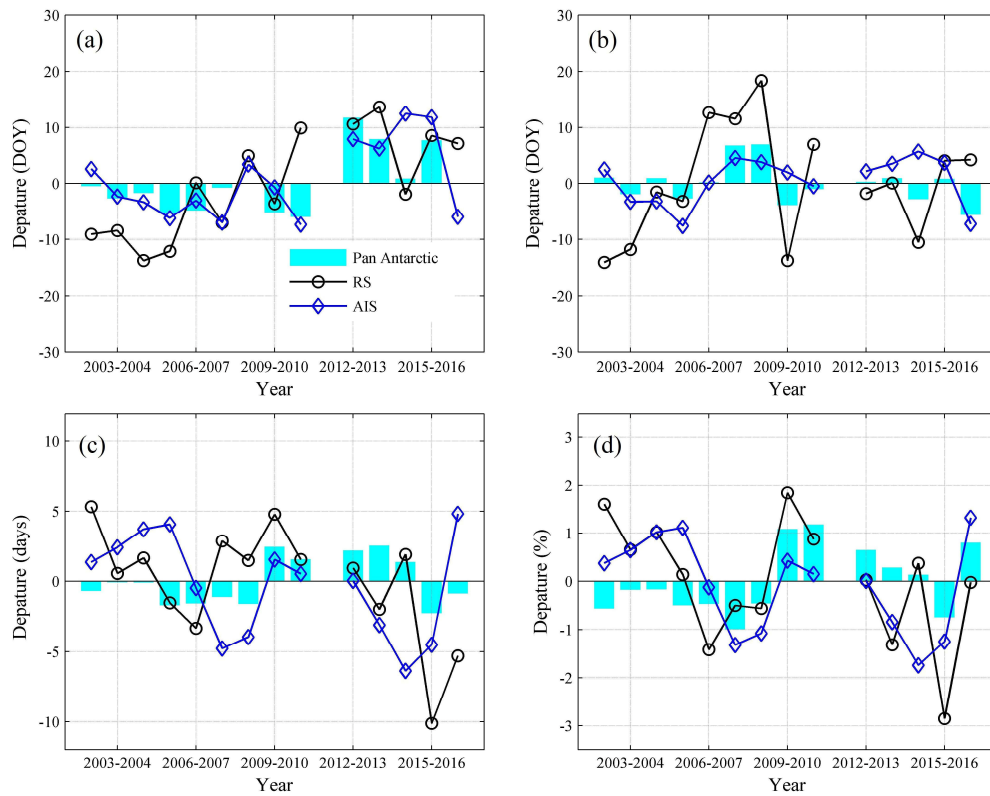
Figure 8. Departure of annual mean (a) EMO, (b) CMO, (c) melting days and (d) MDF for the pan-Antarctic, RS and the AIS.
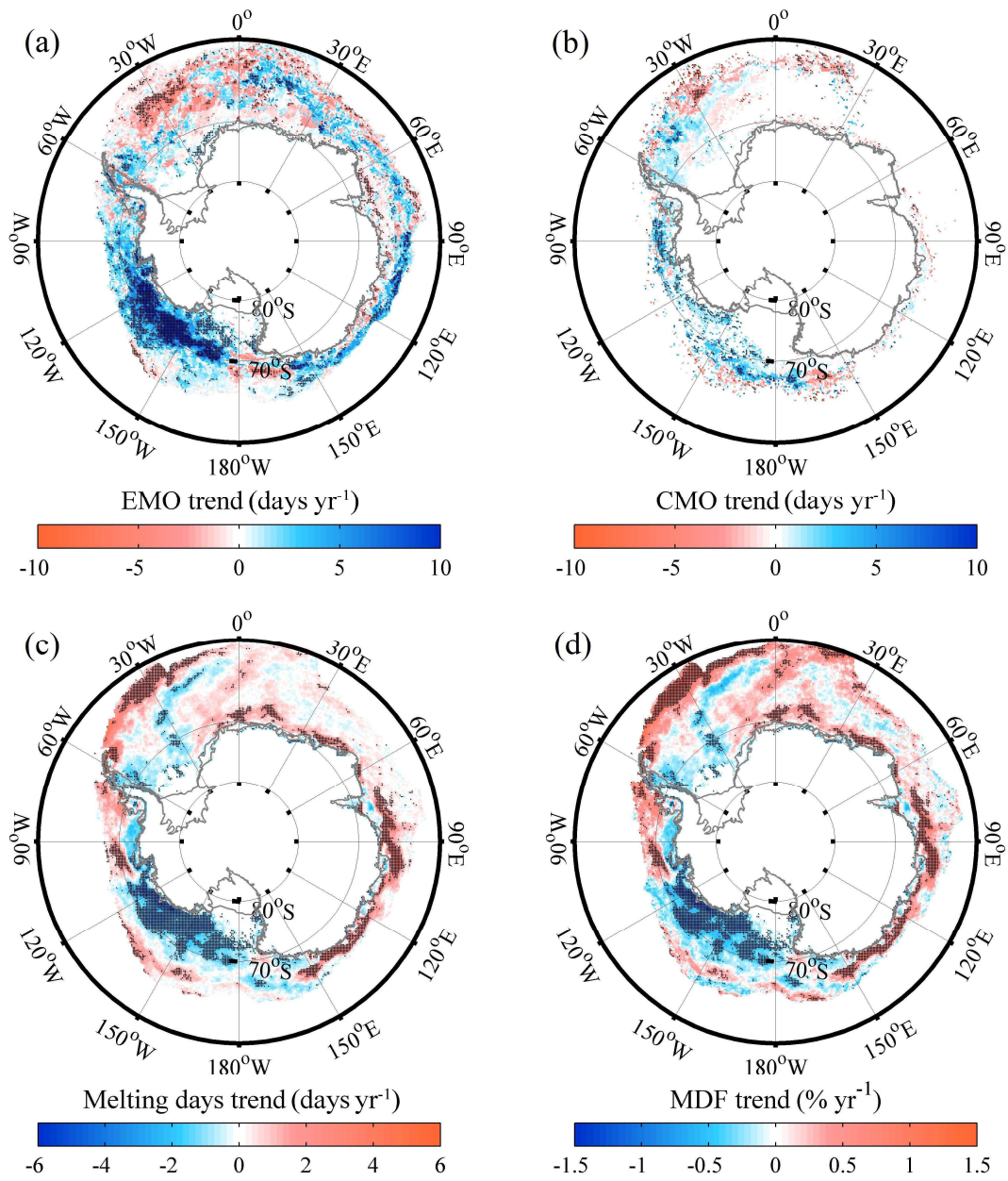
Figure 9. Trends in (a) EMO (b) CMO, (c) melting days and (d) MDF, black points indicate the pixels with trends above 90% confidence level.
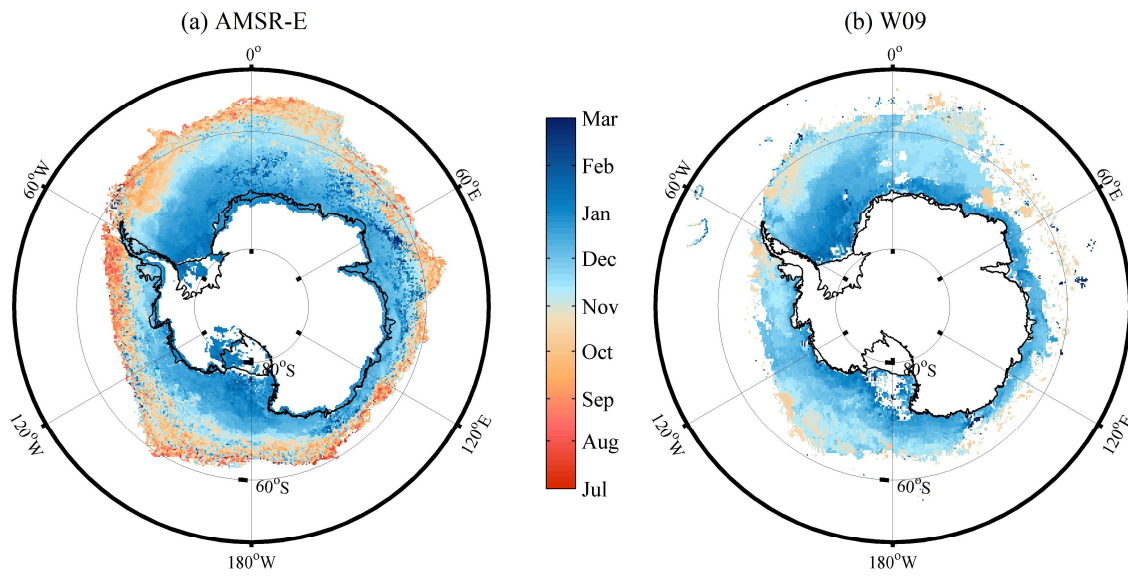
Figure 10. Annual mean CMO derived from (a) AMSR-E and (b) W09 from 2002 to 2008.
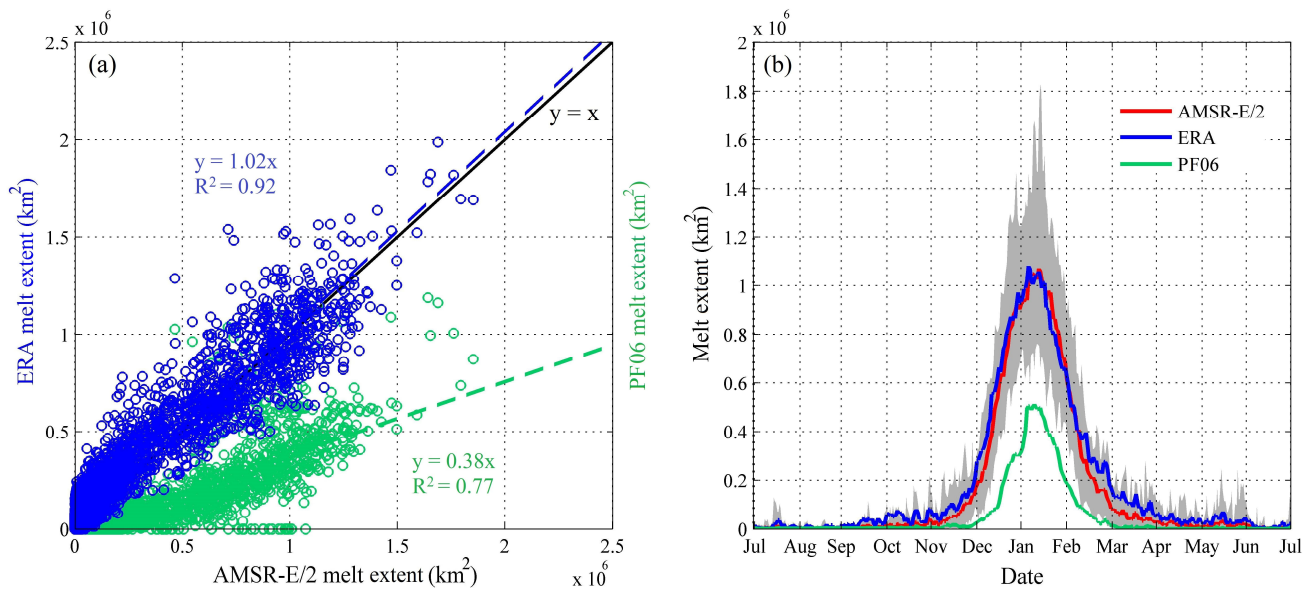
Figure 11. Comparison of AIS melt extent derived by AMSR-E/2, ERA, and PF06 from 2002 to 2017. (a) Scatter plot of daily melt extent, blue circles indicate AMSR-E/2 vs. ERA and green circles indicate AMSR-E/2 vs. PF06. (b) Daily mean melt extent derived by AMSR-E/2 (red line), ERA (blue line) and PF06 (green line), grey shadow indicates the daily maximum and minimum melt extent detected by AMSR-E/2.
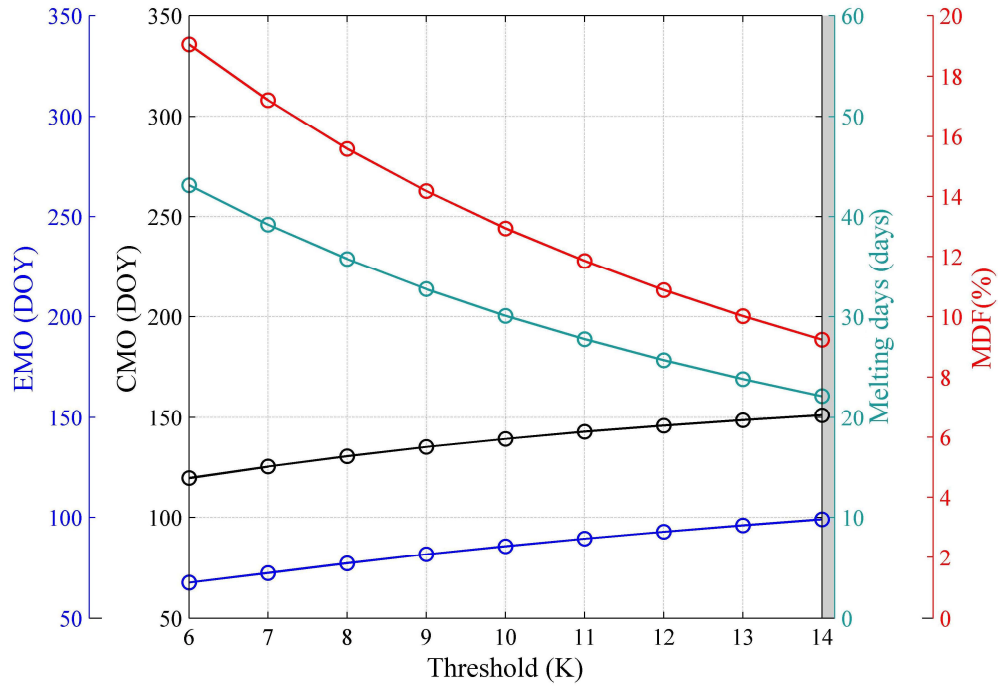
Figure 12. Annual mean EMO (blue dots), CMO (black dots), melting days (cyan dots) and MDF (red dots) with the threshold for AMSR-E/2 DAV36 varying from 6-14 K.
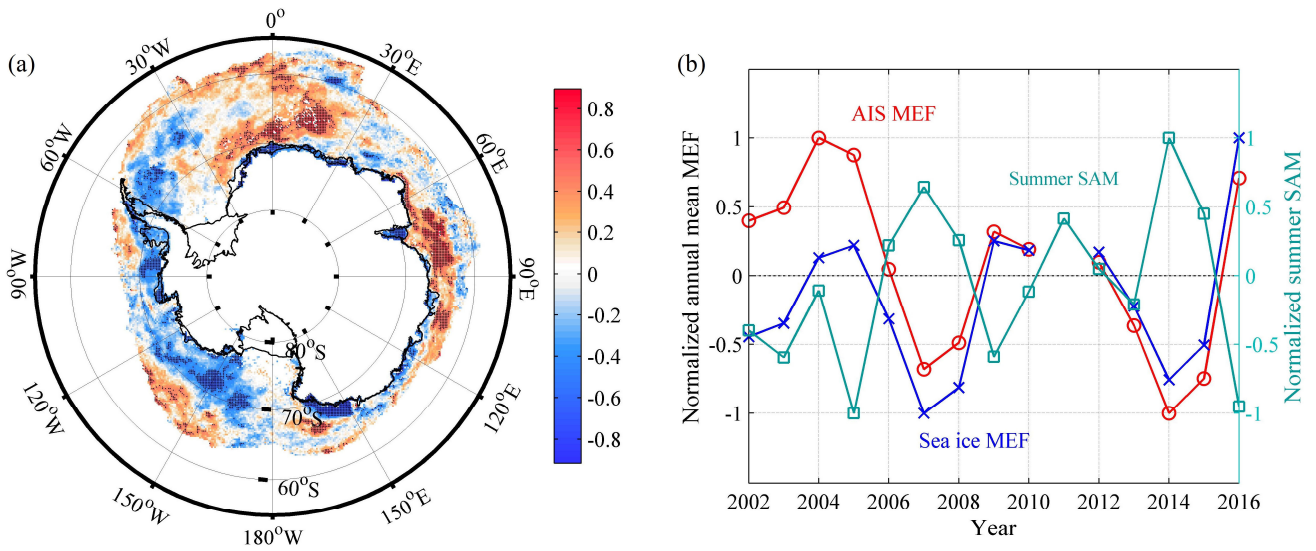
5   **Figure 13. Linkage between pan-Antarctic snowmelt and summer SAM. (a) Correlation coefficient between MDF and summer SAM, black points indicate the trends above 90% confidence level. (b) Comparison of normalized summer SAM (cyan line), normalized annual mean Antarctic sea ice MEF (blue line) and AIS MEF (red line).**